ORIGINAL ARTICLE

Sensitivity Improvements for Picosecond Ultrasonic Thickness Measurements in Gold and Tungsten Nanoscale Films

Jiaqi Dong[1] · **Chengyuan Yao**[2] · **Yuanhao Zhu**[1] · **Shaojie Li**[1] · **Bowen Liu**[1] · **JinTao Fan**[1] · **Chunguang Hu**[2] · **Youjian Song**[1] · **Minglie Hu**[1]

Abstract

Picosecond ultrasonics, as a nondestructive and noncontact method, can be employed for nanoscale metallic film thickness measurements. The sensitivity of the system, which determines the measurement precision and practicability of this technique, is often limited by the weak intensity of the ultrasonic signal. To solve this problem, we investigate the distinct mechanisms involved in picosecond ultrasonic thickness measurement for two types of metals, namely tungsten (W) and gold (Au). For thickness measurement in W films, theory and simulation show that optimizing the pump and probe laser wavelengths, which determine the intensity and shape of the ultrasonic signal, is critical to improving measurement sensitivity, while for Au film measurements, where acoustic-induced beam distortion is dominant, the signal intensity can be optimized by selecting an appropriate aperture size and sample position. The above approaches are validated in experiments. A dual-wavelength pump–probe system is constructed based on a passively mode-locked ytterbium-doped fiber laser. The smoothing method and multipeak Gaussian fitting are employed for the extraction of ultrasonic time-of-flight. Subnanometer measurement precision is achieved in a series of W and Au films with thicknesses of 43–750 nm. This work can be applied to various high-precision, noncontact measurements of metal film thickness in the semiconductor industry.

Highlights

1. Distinct mechanisms between tungsten and gold in picosecond ultrasonic thickness measurement are compared.
2. The system's optimal working point and working area are proposed to enhance ultrasonic signal strength and simplify the measurement process.
3. To the best of our knowledge, we report the widest thin-film measurement range (43–750 nm) in picosecond ultrasonic metal film thickness measurements.

✉ Chunguang Hu
   cghu@tju.edu.cn

✉ Youjian Song
   yjsong@tju.edu.cn

1 Key Laboratory of Opto-Electronic Information Science and Technology of Ministry of Education, School of Precision Instruments and Opto-Electronics Engineering, Tianjin University, Tianjin 300072, China

2 State Key Laboratory of Precision Measuring Technology and Instruments, Tianjin University, Tianjin 300072, China

1 Introduction

Application of various types and thicknesses of coatings to substrates is extensively employed in industry and scientific research. This process effectively combines the physical and chemical properties of materials, leading to a broad range of applications. Monitoring film thickness is critical as it influences the performance of the material and cost control while also ensuring yield.

For metal films, thickness measurement methods can be categorized into (1) destructive [1–3] and (2) nondestructive [4–7]. Although destructive methods provide higher

measurement accuracy, nondestructive methods are preferable for large-scale product monitoring because they avoid material damage. Common nondestructive testing methods include X-ray fluorescence spectroscopy [8, 9], ellipsometry [10], and chromatic confocal [11]. X-ray fluorescence spectroscopy typically has a broad measurement range but requires calibration using standard samples of varying thicknesses and types. Ellipsometry offers high accuracy but necessitates prior modeling, and the metal film layer cannot be excessively thick. Confocal methods can only measure films with a step-like or self-supporting structure. The picosecond ultrasonic technique is a direct, noncontact approach and directly measures thickness using time-of-flight, requiring only the coating film's acoustic velocity without prior information [12]. In addition, it can be seamlessly integrated into the coating system [13].

Figure 1 illustrates this method employing a pump–probe system for measurements. There are two primary stages: (1) Generation of the Ultrasonic Pulse: In Fig. 1a, an ultrafast laser pulse is focused onto the sample surface. The rapid heating of the metal film by the pump laser pulse induces a sudden thermal expansion, generating an ultrasonic pulse that propagates into the material. The resulting ultrasonic pulse can be represented as a superposition of longitudinal plane waves propagating perpendicularly to the surface [14–18]. (2) Detection of the Ultrasonic Pulse: In Fig. 1b, the ultrasonic pulse propagates through the metal film layer at a specific velocity. At the interface between the metal film and substrate, the pulse is either transmitted or reflected due to the contrasting acoustic impedances of the two materials. A portion of the energy is transferred to the substrate, while the residual energy propagates as an echo pulse. As the echo reaches the upper surface of the metal film, it results in a modification of surface reflectivity due to its elastic stress, accompanied by slight deformation. A configurable time delay exists between the probe and the pump lasers. When the delay time exactly corresponds to an integer multiple of the ultrasonic pulse round-trip time, it affects the intensity or phase of the probe laser. The thickness of the sample can be determined from the ultrasonic pulse's time of flight [19–21]. Compared with other approaches, the picosecond ultrasonic method allows direct thickness measurement without preliminary fitting or standard sample calibration. Precise thickness measurement depends solely on the intrinsic ultrasound velocity of the measured sample.

Picosecond ultrasonic thickness measurement in metal films can be classified into two categories based on the differences in detection principles. (1) For metals such as aluminum, tungsten (W), nickel, and others with a strong photoelastic effect, changes in probe laser intensity are detected [22–25]. (2) For noble metals such as gold (Au), copper, and others, phase changes in the probe laser caused by the deformation of the film surface are detected [26–29]. In
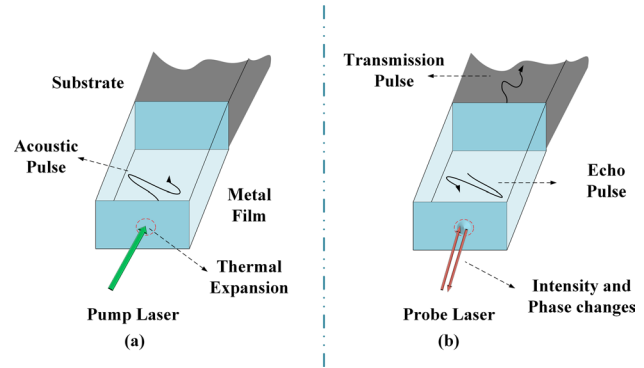

Fig. 1 Pump–probe process in picosecond ultrasonics. **a** Generating the ultrasonic pulse. **b** Detecting the ultrasonic pulse

both cases, the resulting signal is significantly weak, on the order of 10^{-4} to 10^{-6} compared with the DC level. Therefore, improving the signal-to-noise ratio is crucial for determining measurement precision. Studies have been conducted on the impact of laser wavelength [30, 31] and pulse duration [32] on picosecond ultrasonics, and different methods have been developed to enhance measurement sensitivity, such as asynchronous optical sampling [33–36], double-frequency modulation [37], and nonlinear wave measurement [38].

This study focuses on W and Au, two representative metals, for picosecond ultrasonic thickness measurements. First, we simulate the patterns of ultrasonic signals in W and discuss the significant impact of laser wavelength. Afterward, we determine the optimal working point and working area to improve the ultrasonic signal intensity for Au film measurements. Subsequently, we build a dual-wavelength pump–probe system using an ytterbium (Yb)-doped fiber laser to measure the thickness and validate the simulations. We also discuss the optimal method for data processing to improve the measurement stability of the system. Using the picosecond ultrasonic technique, a set of W and Au films with thicknesses of 43–750 nm are characterized with single nanometer precision, which is so far the widest thin-film measurement range.

2 Principle and Simulation

Despite using picosecond ultrasonic technology, there are differences in measurement principles between Au and W. W exhibits a strong photoelastic effect, where the stress generated by the ultrasonic pulse causes changes in the real part ρ of the reflection coefficient, also known as reflectivity. Thus, variations in the probe laser intensity can be detected to reconstruct the ultrasonic signal. However, due to its larger acoustic pulse duration, Au induces a minor change in the real part ρ of the reflection coefficient. This change can be

disregarded when compared with the phase change brought about by the surface displacement. In this case, detecting the change in the imaginary part φ of the reflection coefficient becomes necessary.

2.1 Picosecond Ultrasonics on W

The thickness of W is determined by measuring the change in reflectivity $\delta R/R_0$. According to previous work [20], this is expressed as

$$\frac{\delta R}{R_0} = \text{Re}\left[\frac{8i\tilde{n}}{\left(1-\tilde{n}^2\right)\left(\tilde{n}^2+\left(\frac{\kappa_0\lambda}{\lambda_0}\right)^2\right)}\frac{d\tilde{n}}{d\eta}(A+B)\right] \quad (1)$$

$$A = \frac{\kappa_0\lambda}{\lambda_0}e^{-\frac{v_1|t|}{\zeta_0}} \qquad B = i\tilde{n}e^{2iknv_1|t|}e^{\frac{-v_1|t|}{\zeta}}$$

The pump laser wavelength λ_0 corresponds to the refractive index $\widetilde{n_0} = n_0 + \kappa_0$ and optical absorption depth ζ_0. Similarly, the probe laser wavelength λ corresponds to the refractive index $\tilde{n} = n + \kappa$ and optical absorption depth ζ. The photoelastic constant of the material is $d\tilde{n}/d\eta$, and v_1 is the longitudinal velocity of the ultrasonic pulse in the material. Equation (1) comprises two terms: the first term is transient with a decay time $\tau = \zeta_0/v_1$, and the second term is an oscillatory term with frequency $f_n = 2nv_1/\lambda$ and decay time $\tau_n = \zeta/v_1$. The ratio of these two terms is significantly influenced by the optical constants. Consequently, different wavelengths and materials yield distinct acoustic signals.

For a film layer composed of a specific material, the transient and oscillatory terms, due to different wavelengths, can have the same or opposite signs. This can result in the intensity of the total term being either positive or negative. In certain instances, the cancellation between the two terms obscures the phenomena of picosecond ultrasonics. This explains the reported experimental results [31] for Si$_3$N$_4$. At a particular wavelength, no picosecond ultrasonic signal is observed, while on both sides of that wavelength, ultrasonic signals of the opposite sign are obtained.

Hence, it is crucial to select suitable pump and probe laser wavelengths, in conjunction with various optical constants, before measuring different metals. Herein, a pump laser wavelength of 515 nm and a probe laser wavelength of 1,030 nm were selected. Figure 2 shows the simulation results of the W film. The total signal exhibits a central peak flanked by two troughs. Simulating the pulse shape aids in the subsequent signal processing and improves the precision of the measurement results.

Assuming the measured film thickness $d = 250$ nm and the longitudinal speed of the ultrasonic pulse $v_1 = 5$ nm/ps,
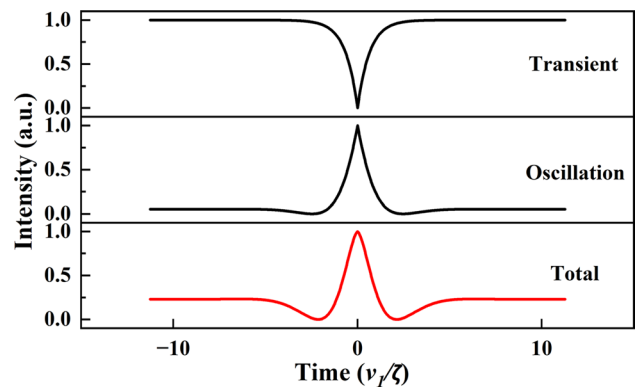

Fig. 2 Shapes of the transient, oscillation, and total terms of the simulated ultrasonic signal in W ($\lambda_0 = 515$ nm, $\lambda = 1030$ nm)
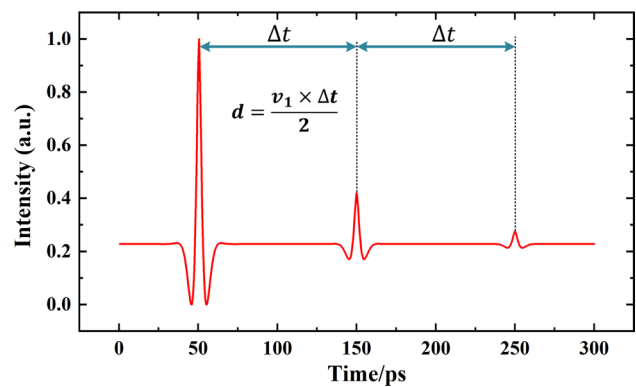

Fig. 3 Simulation results of the detection signal intensity versus delay time (ignoring the first strong reflection peak and thermal background)

the time interval between adjacent pulses is 100 ps. The simulated time-domain curve is shown in Fig. 3. Each ultrasonic signal is equally spaced in time with decreasing intensity. Film thickness is determined by calculating the time difference between the peaks of neighboring pulses.

2.2 Picosecond Ultrasonics on Au

For Au films, the intensity change of the probe laser is extremely weak, so it is necessary to detect the optical path length changes due to surface deformation. While these changes can typically be captured through interference and deflection techniques, such methods augment the complexity of the system. We employ the reported beam distortion detection method [27] to measure changes in the reflection coefficient's imaginary part.

Figure 4 shows the principle of beam distortion detection. In the picosecond ultrasonic system, the beam must be focused onto the sample to ensure high fluence
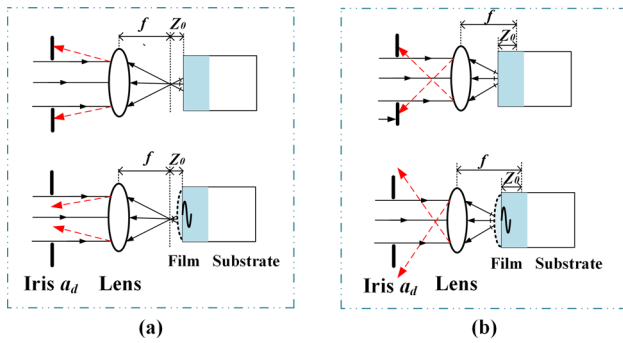
Fig. 4 Principle of beam distortion detection. **a, b** The upper inset shows undistorted beam transmission without an ultrasonic pulse, while the lower inset depicts distorted beam transmission with an ultrasonic pulse

excitation. The sample is usually positioned close to the lens's focus, $D \approx f + Z_0$, where Z_0 is the distance between the sample and the lens's focal plane. In the upper inset of Fig. 4a, b, the thin film is intentionally placed slightly out of the focus where Z_0 is positive (negative). Therefore, the reflected laser beam by the thin film is diverged. Here, an iris diaphragm is positioned at a certain reference plane, with the aperture size adjusted such that part of the reflected beam is blocked, where a_d is the aperture size of the iris. Then, when the ultrasonic pulse reaches the metal surface, surface deformation occurs. Given that the distance between the thin film and the lens changes, the reflected beam will converge (diverge), as shown in the lower inset of Fig. 4a, b. Therefore, the intensity of the reflected laser entering the iris is increased (decreased), producing a peak (dip) in the trace of detection signal intensity versus delay time. This setup effectively converts phase measurements into intensity measurements.

Due to the difference in sample position, the beam is more focused after surface deformation in (a), and the beam is more divergent in (b).

The expression for the relative change in laser power $\Delta P/P_0$ represents a beam distortion rate S_0. A larger beam distortion rate reflects a higher ultrasonic signal measurement sensitivity. S_0 is expressed as

$$S_0 = \frac{\Delta P}{P_0} = 4\frac{a_d^2}{a^2}\exp\left(-\frac{2a_d^2}{a^2}\right)\frac{2A_0Z_0}{\omega_p^4(z_0)} \quad (2)$$

In Eq. (2), a is the undistorted radius of the probe spot at the location where the iris is placed. Z_0 takes a positive value when the sample is on the right side of the focus. A_0 is proportional to the instantaneous displacement $u(t)$ of the sample surface. Usually, the sample is expanded, and A_0 takes a negative value. $\omega_p(z_0) = \omega_{p0}\sqrt{1 + \left(z_0\lambda_0/\pi\omega_{p0}^2\right)^2}$,

where ω_{p0} is the waist radius of the pump laser and λ_0 is the wavelength of the pump laser.

As Eq. (2) suggests, two variables must be calibrated to attain maximal signal intensity compared with the measurement of W films. The variables are (1) the iris's aperture a_d and (2) the displacement of the sample relative to the focal plane Z_0. Their impacts are discussed separately below to determine the optimal working point and working area for beam distortion measurement.

The iris's aperture is typically estimated via simulation, but it requires adjustment by a power meter before each measurement. The process is simplified below. Note that when the probe laser lags behind the pump laser, there exists not only a beam distortion signal but also a thermal background signal. This background signal is caused by the absorption of hot electrons and lattice heat at $t = 0$. Over a certain period, the thermal background signal of the Au film remains constant P_{h1}. The detection intensity of P_h depends solely on the spot size a and aperture size a_d and can be expressed as

$$\frac{P_h}{P_0} = \frac{P_{h1}}{P_0} \times \left(1 - \exp\left(-\frac{2a_d^2}{a^2}\right)\right) \quad (3)$$

Therefore, combining Eqs. (2) and (3), we obtain a beam distortion rate with background, expressed as S. This is the final detection signal.

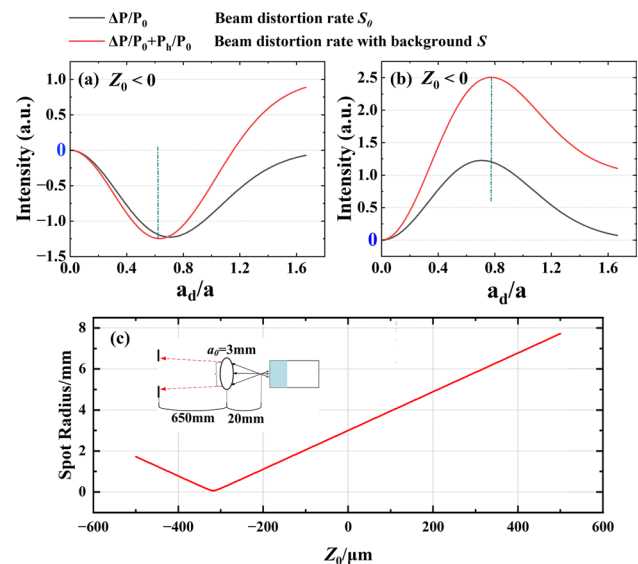$$S = \frac{P_h}{P_0} + \frac{\Delta P}{P_0} \quad (4)$$

Fig. 5 Beam distortion rate S_0 and beam distortion rate with background S versus aperture size a_d. **a** Case $Z_0 > 0$, sample on the right side of the focus. **b** Case $Z_0 < 0$, sample on the left side of the focus. **c** Simulated laser spot size at the diaphragm with Z_0

P_h/P_0 and $\Delta P/P_0$ are essentially of the same order of magnitude. Figure 5 shows the relationship between S and S_0 with respect to the aperture diameter when the ultrasonic pulse reaches the sample surface for cases when $Z_0 < 0$ and $Z_0 > 0$. Figure 5 demonstrates that maximum beam distortion exists either when $Z_0 > 0$ or $Z_0 < 0$, resulting in the strongest signal contrast in the trace of detection signal intensity versus delay time. Experimentally, only the beam distortion rate with background S can be measured. However, because the local maxima of S and S_0 are close, as shown in Fig. 5, we can take the measured local maximum of S as the optimal working point to determine the aperture diameter.

In practice, $Z_0 > 0$ is chosen to determine the maximum beam distortion. The reason is twofold. First, the intensities of S and S_0 reach the maximum almost at the same time by decreasing aperture size, as shown in the guide lines in Fig. 5a and Fig. 5b, respectively. However, the maxima of S and S_0 have almost the same value for $Z_0 > 0$. This significantly facilitates the process of locating the system's optimal working point. Second, larger beam spots are favorable for aligning the optic. Figure 5c shows the simulated laser spot size at the diaphragm with Z_0 by using the ray transfer matrix. It is observed that the spot expands to an acceptable size when $Z_0 > 0$ but the spot is much smaller when $Z_0 < 0$. To achieve a large beam distortion rate, a small diaphragm aperture size is needed, which may be limited by the mechanical tolerance of the diaphragm.

We further investigate the impact of the sample's distance from the focal plane, denoted as Z_0, on the maximal signal intensity. The relationship between the beam distortion rate S_0 and Z_0 is depicted in Fig. 6. The graph reveals that $S_0 = 0$ when $Z_0=0$. There are two maxima, namely, that when $Z_0 > 0$ and that when $Z_0 < 0$. After the maximum signal, the intensity returns to 0 due to the decrease in average fluence excitation.
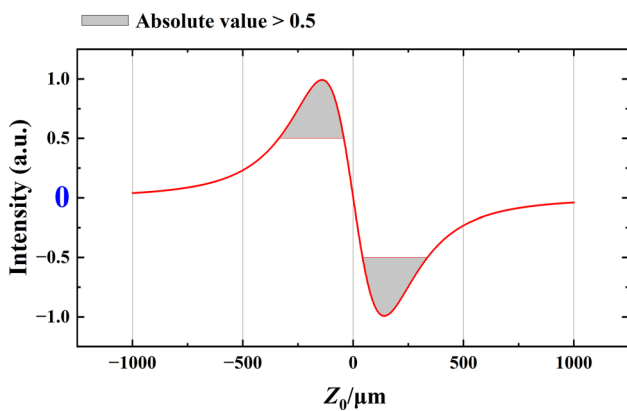

Fig. 6 Beam distortion signal intensity versus sample distance from the focal plane Z_0. The shaded areas on the graph represent regions where the absolute value of the intensity exceeds 0.5
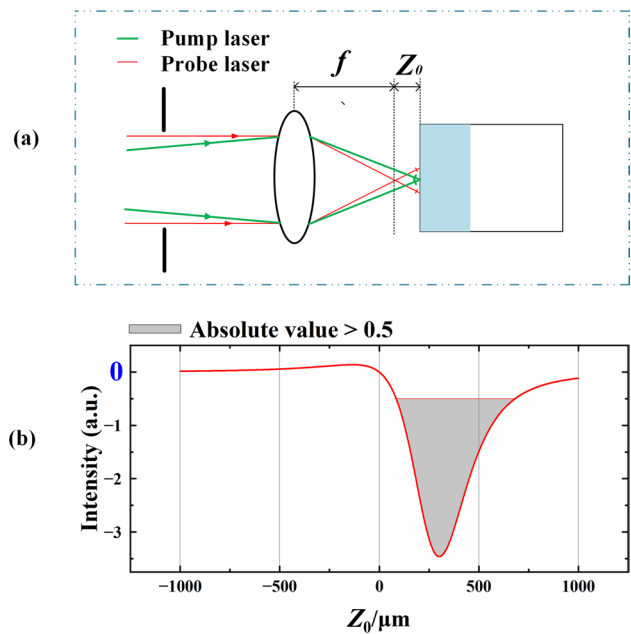

Fig. 7 Scenario of focal separation between pump and probe lasers. **a** Schematic representation of the focusing of the pump and probe lasers. **b** Beam distortion signal intensity versus sample distance from the focal plane of the probe laser Z_0. The shaded areas on the graph represent regions where the absolute value of the intensity exceeds 0.5

In the above discussion, the pump and probe lasers are spatially overlapped. Note that the pump laser is not perfectly focused on the metal film ($Z_0 \neq 0$), as shown in Fig. 4, the efficiency for ultrasonic signal generation is low. To overcome this problem, as shown in Fig. 7a, we further optimized the focusing of the pump and probe lasers by intentionally separating their focus. After the lens focuses the lasers, the pump beam waist is positioned on the right side of the probe beam waist. Z_0 is the distance between the sample and the focal plane of the probe laser. Figure 7b illustrates the relationship between the intensity of the beam distortion signal and Z_0. The distortion signal in the region where $Z_0 > 0$ is amplified due to the more efficient use of average fluence. Under these circumstances, using the $Z_0 > 0$ area for measurement allows a larger working area of Z_0 and results in increased signals (three times larger than those in Fig. 6).

3 Experiments and Data Analysis

3.1 Experimental Setup

Figure 8 illustrates the optical structure of the picosecond ultrasonic thickness measurement setup. The employed light source is a Yb-doped fiber laser (BWT, BFL-1030-10LEW) featuring a central wavelength of 1032 nm and a

Fig. 8 Optical structure of the dual-wavelength pump-probe system. HWP: half-wave plate, PBS: polarizing beam splitter, QWP: quarter-wave plate, DM: dichroic mirror, AOM: acousto-optic modulator, PD: photodetector, LBO: lithium triborate, L1, L2, L3: lens, where L1 and L2 are plano-convex lenses and L3 is an aspherical lens
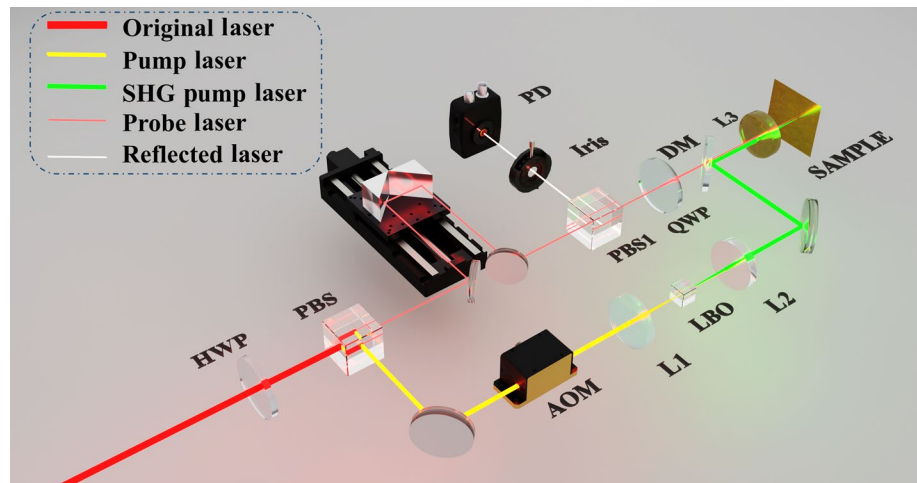
pulse duration of 220 fs. It operates at a repetition rate of 48.99 MHz. Initially, a half-wave plate (HWP) and a polarizing beam splitter (PBS) are used to divide the optical comb into pump and probe paths. The pump laser undergoes low-frequency modulation using an acousto-optic modulator (AOM) and is frequency-doubled to a 516 nm green laser via a lithium triborate (LBO) crystal. Lenses L1 and L2 are utilized to focus and collimate the pump laser. For the probe laser, the time delay is realized by the motorized displacement platform. Afterward, the probe laser passes through the quarter-wave plate (QWP). The two lasers are combined at a dichroic mirror (DM) and focused on the sample using lens L3. The pump laser operates at approximately 50 mW and the probe laser at approximately 600 μW. The reflected probe laser undergoes QWP twice, resulting in a polarization state orthogonal to the initial state. This probe laser is reflected to a photodetector (PD) via the PBS1, generating detection signals.

Due to the low intensity of the ultrasonic signal, it is necessary to use a lock-in amplifier (LIA) for signal extraction. Initially, a signal generator is employed to stimulate the AOM to produce sinusoidal modulation at a frequency of 800 kHz. The sinusoidal signal also serves as a reference for the LIA to extract the corresponding frequency components from the PD. The RC time constant of the LIA filter is set at 300 ms. The total time delay introduced by the displacement platform amounts to 330 ps, with a time step of 0.2 ps. The maximum measurement duration is approximately 400 s.

3.2 Experiment on Tungsten

During W film thickness measurement, we maintain the iris diaphragm in a fully open state, and the aperture size significantly exceeds the beam spot radius. The lens L2 is adjusted to ensure the pump and probe laser focus are in the same position. The sample is W metal coated on silicon (Si) (100).

The time-domain signal curve is depicted in Fig. 9. The intensity of the detected signal initially increases rapidly, then diminishes, and finally stabilizes, forming a slow-varying thermal background signal. Ultrasonic signals are produced when the ultrasonic pulse is transmitted onto the W film's surface. These signals have the same time interval Δt and a decreasing intensity. It can be seen from the zoomed-in figure that the ultrasonic signals are in the form of tripoles, which is consistent with the simulation results in Sect. 2.1.

Figure 10 displays the signal curve after removing the first peak and the thermal background signal. The inset displays the spectrum of a single ultrasonic signal, with a central frequency approximating 62 GHz. To calculate the thickness, it is crucial to determine the precise timing corresponding to the center of each ultrasonic peak. Focusing on the central portion of each signal, the full width at half-maximum is roughly 5 ps. The peaks are characterized by narrow pulse widths and high contrast, allowing peak extraction through general curve smoothing techniques. Using the
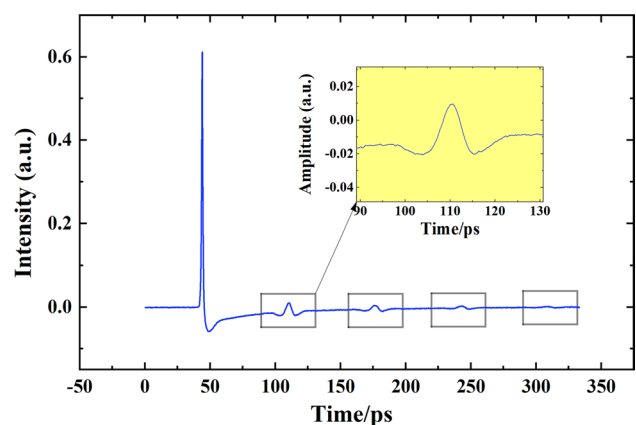

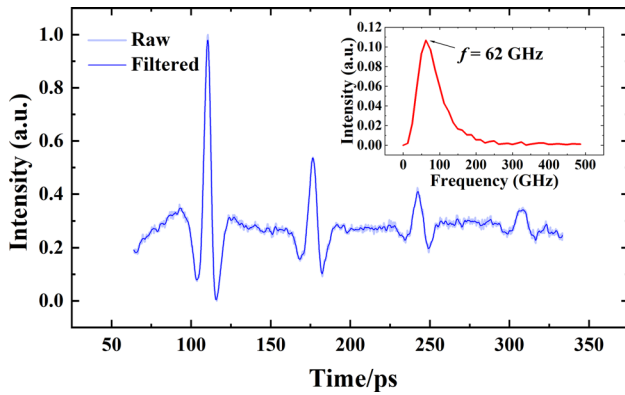**Fig. 9** Detection signal intensity versus delay time for 172 nm W film measurements

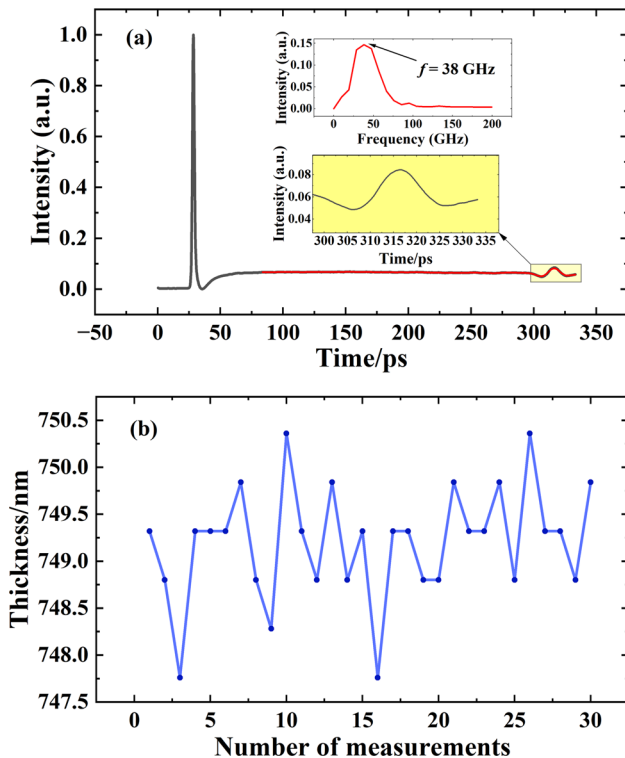**Fig. 10** Raw and filtered results of the ultrasonic signal in W film measurements

Fig. 11 Measurement results of the 749 nm W film. **a** Detection signal intensity versus delay time under a single measurement. **b** Results of 30 thickness measurements

Savitzky–Golay filter with a window of 16, the average of 10 thickness measurements was 172.07 nm with a standard deviation of 0.59 nm.

To ensure the consistency of the experimental results, we measured various thicknesses of the film layers. Due to the limitations of the range of the displacement stage, the maximum measured thickness was 800 nm, with its time-domain

measurement curve depicted in Fig. 11a. The curve indicates that the emergence of the adjacent ultrasonic signal is significantly delayed due to the increased thickness. However, the shape remains unchanged, maintaining the characteristics of a tripolar pulse with a center frequency of 38 GHz. In Fig. 11b, the average thickness from 30 measurements was 749.20 nm with a standard deviation of 0.62 nm.

The sample was calibrated by the Shenzhen Academy of Metrology & Quality Inspection (SMQ) using a contact profilometer (Form Talysurf PGI 830), which yielded a measurement of 730 nm, showing a deviation of 2.6% compared with that by the picosecond ultrasonic method.

3.3 Experiment on Au

The beam distortion detection technique is used to measure the Au film. Au films with nominal thicknesses of 50, 100, and 200 nm coated on a SiO_2/Si layer is utilized. The results of these measurements are presented in Fig. 12 as the original measurement curve (black line) and the filtered curve (red line). Figure 12a–c. are the measured curves obtained with the same system configuration presented in Sect. 3.2. From these curves, the detection signals rise rapidly when the pump and probe pulses meet, and then they tend to stabilize, which is basically a constant-value thermal background signal. These graphs do not display any ultrasonic signals, and the time-domain curves are essentially identical. Conversely, Fig. 12d–f. show the results when the iris aperture's size is adjusted at the optimal working point following the method in Sect. 2.2. The pump beam waist is positioned on the right side of the probe beam waist by adjusting lens L2, following Fig. 7 in Sect. 2.2. From these curves, the detection signals also rise rapidly when the two pluses meet, and then their intensity decreases rapidly due to the beam distortion signal. Subsequently, distinct periodic ultrasonic signals emerge.

The measurement results demonstrate that the system performs better when operating at its optimal working point, thus proving the analysis in Sect. 2.2. The insets in Fig. 12d–f. display the corresponding spectral diagrams of the ultrasonic signals. The ultrasonic pulse's central frequency decreases with increasing Au film thickness.

For the measurement of Au film thickness, the resolution is also an issue to be considered. From the time-domain measurement curve, the measured signal for the Au film is distinct from that of the W film. Due to the longer wavelength of the ultrasonic pulse in the Au film, the superposition of continuous ultrasonic signals is observed rather than the independent situation of the W film. Furthermore, due to the low center frequency of the ultrasonic pulse, the signal is more vulnerable to noise interference. To illustrate this issue, we used an 80 nm Au film and applied the smoothing method from Sect. 3.2. The results of 15 measurements produced a standard
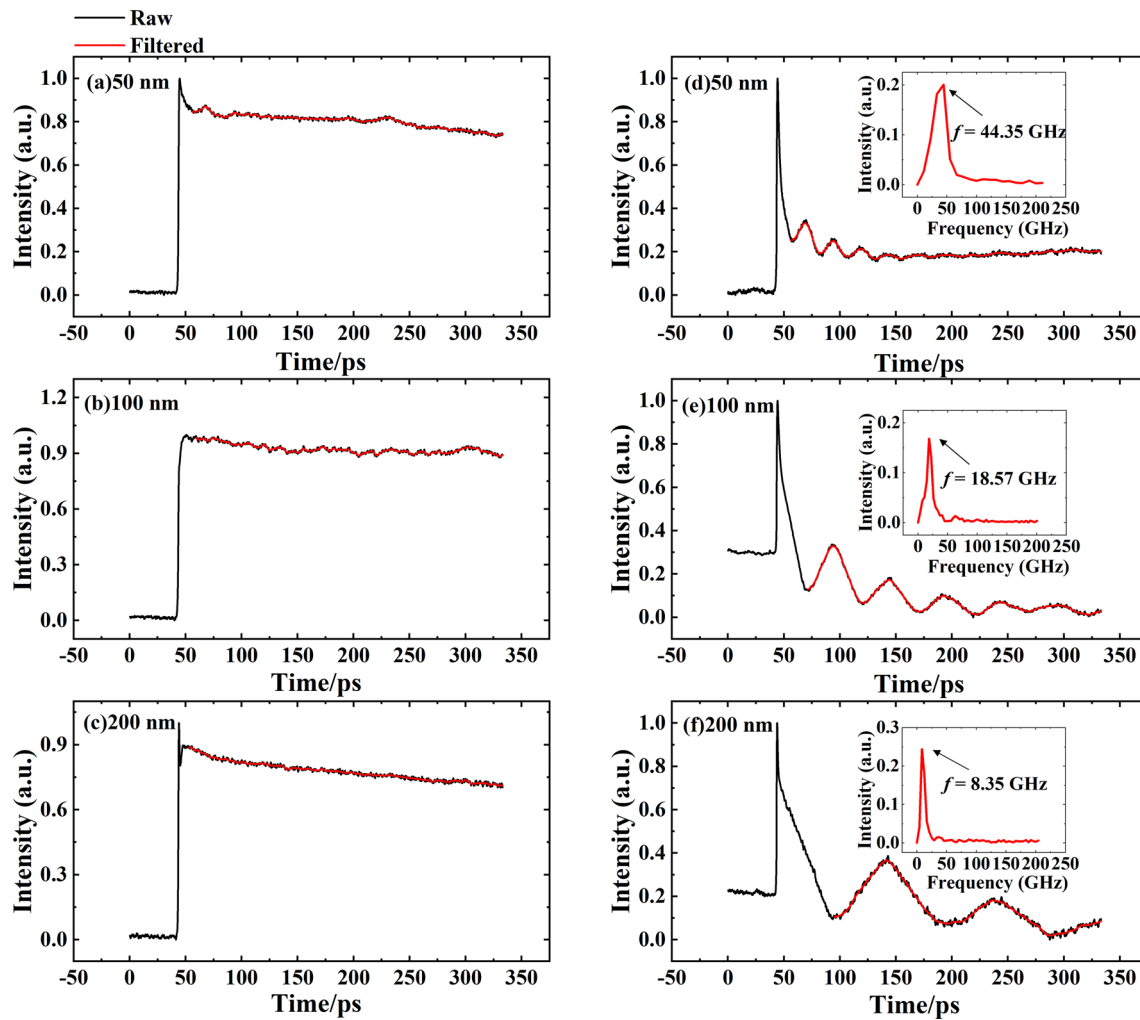
Fig. 12 Detection signal intensity versus delay time for 50, 100, and 200 nm Au film measurements. **a–c** Measurement results when the aperture is at full opening. **d–f** Measurement results when the aperture is at the optimal working point

deviation of 2.87 nm, suggesting that noise has significantly deteriorated the measurement accuracy. Because the curve results from a combination of several impulse responses, we recommend employing a multipeak Gaussian fitting approach, which avoids the problem of frequent changes in the smoothing scheme due to thickness changes. Figure 13a shows the fitting result, demonstrating good agreement between the raw data and the fitted curve. The standard deviation of the measurements from 15 independent trials was only 0.99 nm. In Fig. 13b, the actual measured results using this method for the three thicknesses of the Au films were 42.35, 82.29, and 161.66 nm. The calibrated results from SMQ were 43.67, 81.00, and 165.33 nm, with deviations of 1.32, 1.29, and 3.67 nm, respectively.

4 Summary

Herein, we discuss in detail the application of picosecond ultrasonic technology in the field of metal film thickness measurement with the aim of enhancing system sensitivity to improve measurement precision. The main findings are in three aspects:

(1) Measurement of various metal films. Our study mainly focused on two types of metals: W detects the intensity change of the reflected probe laser due to the photoelastic effect, while Au detects metal surface deformation using the beam distortion detection method. This study simulated the theoretical generation of ultrasonic signals for the two metals and experimentally validated it.
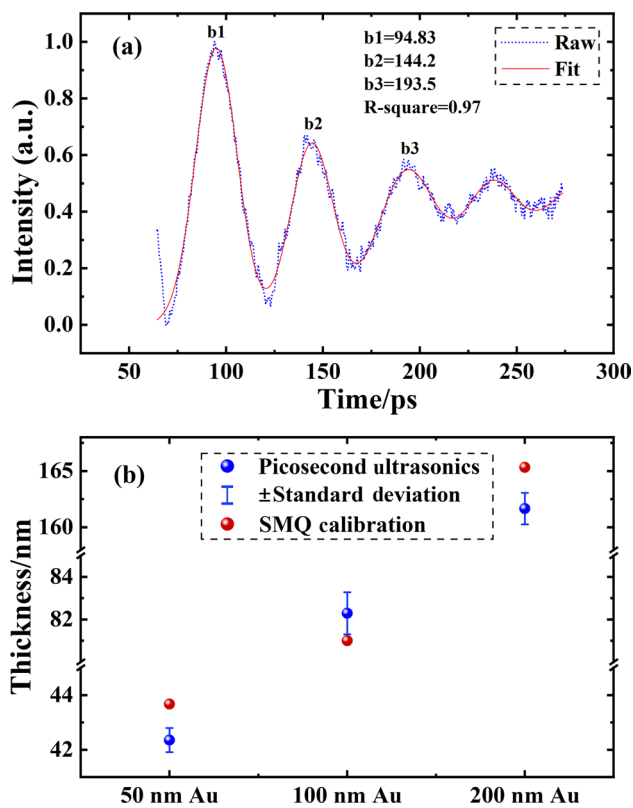
Fig. 13 Thickness measurement results of the Au films. **a** Results of the multipeak Gaussian fitting approach. **b** Comparison between picosecond ultrasonic results and SMQ calibration results

(2) Measurement sensitivity improvement method. The measurements of the W film focused on the impact of laser wavelength on the ultrasonic signal shape. The experimental results were in agreement with the simulations, as well as in the case of different thicknesses. For the measurement of Au film thickness, we proposed selecting the optimal working point and working area, reducing the adjustment difficulty. We also expanded the working area and enhanced the intensity of the ultrasonic signal.

(3) Realization of high-precision measurement over a wide range. The system measured metal film thicknesses of 43–750 nm. Employing smoothing methods and multipeak Gaussian fitting, the standard deviation of the measurement results reached the single nanometer scale. The results closely align with thicknesses calibrated by professional organizations.

The proposed method improved measurement sensitivity for picosecond ultrasonics. However, optical path adjustment still depends on experience to some extent. Optimal parameters such as laser power and beam alignment still require trial and error. Meanwhile, the current system employs a mechanical delay line that limits the thickness measurement range and measurement speed. Meanwhile, the utilization of a dual-comb asynchronous sampling system contributes to substantially improved measurement range and reduced measurement time. The proposed sensitivity improvement method can also be applicable to the ASOPS system, which allows a broader application of picosecond ultrasonic thin-film thickness measurement in the future.

Author Contributions All authors read and approved the final manuscript.

Data Availability The data that supports the findings of this study are available from the corresponding author (Dr. Youjian Song) upon reasonable request.

Declarations

References

1. Giurlani W, Berretti E, Innocenti M, Lavacchi A (2020) Measuring the thickness of metal coatings: a review of the methods. Coatings 10(12):1211. https://doi.org/10.3390/coatings10121211
2. Lindner M, Schmid M (2017) Thickness measurement methods for physical vapor deposited aluminum coatings in packaging applications: a review. Coatings 7(1):9. https://doi.org/10.3390/coatings7010009
3. Misumi I, Kizu R, Itoh H et al (2022) Research activities of nanodimensional standards using atomic force microscopes, transmission electron microscope, and scanning electron microscope at the national metrology institute of Japan. Nanomanuf Metrol 5(2):83–90. https://doi.org/10.1007/s41871-021-00119-1
4. Paramsamy Kannan V, Barile C (2022) Nondestructive evaluation of material surfaces: theory, techniques, and applications. Coatings 12(7):960. https://doi.org/10.3390/coatings12070960

5. Whiteside PJ, Chininis JA, Hunt HK (2016) Techniques and challenges for characterizing metal thin films with applications in photonics. Coatings 6(3):35. https://doi.org/10.3390/coatings6030035

6. Yuan Y, Yao C, Shen W, Hu X, Hu C (2022) Polarization measurement method based on liquid crystal variable retarder (LCVR) for atomic thin-film thickness. Nanomanuf Metrol 5(2):159–166. https://doi.org/10.1007/s41871-022-00131-z

7. Fan Z, Hu X, Gao RX (2022) Indirect measurement methods for quality and process control in nanomanufacturing. Nanomanuf Metrol 5(3):209–229. https://doi.org/10.1007/s41871-022-00148-4

8. Rong J, Zhu X, Wang K, Du H (2019) Parameters selection for different metals in coating thickness measurement using x-ray fluorescence analysis. In: 9th international symposium on advanced optical manufacturing and testing technologies: subdiffraction-limited plasmonic lithography and innovative manufacturing technology. 10842: 203–209. https://doi.org/10.1117/12.2504972

9. Takahara H (2017) Thickness and composition analysis of thin film samples using FP method by XRF analysis. Rigaku J 33:17–21

10. Zhu XD, Zhang RJ, Zheng YX, Wang SY, Chen LR (2019) Spectroscopic ellipsometry and its applications in the study of thin film materials. Chin Opt 12(6):1195–1234. https://doi.org/10.3788/CO.20191206.1195

11. Li J, Zhu X, Du H, Ji Z, Wang K, Zhao M (2021) Thickness measurement method for self-supporting film with double chromatic confocal probes. Appl Opt 60(30):9447–9452. https://doi.org/10.1364/AO.432384

12. Thomsen C, Grahn HT, Maris HJ, Tauc J (1986) Surface generation and detection of phonons by picosecond light pulses. Phys Rev B 34(6):4129. https://doi.org/10.1103/PhysRevB.34.4129

13. Rahman MM, Elsayed-Ali HE (2021) On-line thin film thickness monitor by pulsed laser photoacoustics. Opt Lasers Eng 139:106482. https://doi.org/10.1016/j.optlaseng.2020.106482

14. Thomsen C, Strait J, Vardeny Z, Maris HJ, Tauc J, Hauser JJ (1984) Coherent phonon generation and detection by picosecond light pulses. Phys Rev Lett 53(10):989. https://doi.org/10.1103/PhysRevLett.53.989

15. Wright OB, Perrin B, Matsuda O, Gusev VE (2001) Ultrafast carrier diffusion in gallium arsenide probed with picosecond acoustic pulses. Phys Rev B 64(8):081202. https://doi.org/10.1103/PhysRevB.64.081202

16. Matsuda O, Tachizaki T, Fukui T, Baumberg JJ, Wright OB (2005) Acoustic phonon generation and detection in GaAs/ Al 0.3 Ga 0.7 As quantum wells with picosecond laser pulses. Phys Rev B 71(11):115330. https://doi.org/10.1103/PhysRevB.71.115330

17. Ruello P, Gusev VE (2015) Physical mechanisms of coherent acoustic phonons generation by ultrafast laser action. Ultrasonics 56:21–35. https://doi.org/10.1016/j.ultras.2014.06.004

18. Rogers JA, Maznev AA, Banet MJ, Nelson KA (2000) Optical generation and characterization of acoustic waves in thin films: Fundamentals and applications. Annu Rev Mater Sci 30(1):117–157. https://doi.org/10.1146/annurev.matsci.30.1.117

19. Hurley DH (2019) Pump-probe laser ultrasonics: characterization of material microstructure. IEEE Nanotechnol Mag 13(3):29–38. https://doi.org/10.1109/MNANO.2019.2904772

20. Matsuda O, Larciprete MC, Voti RL, Wright OB (2015) Fundamentals of picosecond laser ultrasonics. Ultrasonics 56:3–20. https://doi.org/10.1016/j.ultras.2014.06.005

21. Vital-Juarez A, Roffi L, Desmarres JM, Devos A (2022) Picosecond acoustics versus tape adhesion test: confrontation on a series of similar samples with a variable adhesion. Surf Coat Technol 448:128926. https://doi.org/10.1016/j.surfcoat.2022.128926

22. Rossignol C, Perrin B (2005) Interferometric detection in picosecond ultrasonics for nondestructive testing of submicrometric opaque multilayered samples: TiN/AlCu/TiN/Ti/Si. IEEE Trans Ultrason Ferroelectr Freq Control 52(8):1354–1359. https://doi.org/10.1109/TUFFC.2005.1509794

23. Saito T, Matsuda O, Wright OB (2003) Picosecond acoustic phonon pulse generation in nickel and chromium. Phys Rev B 67(20):205421. https://doi.org/10.1103/PhysRevB.67.205421

24. Kobecki M, Tandoi G, Gaetano Di et al (2020) Picosecond ultrasonics with miniaturized semiconductor lasers. Ultrasonics 106:106150. https://doi.org/10.1016/j.ultras.2020.106150

25. Dehoux T, Audoin B (2012) Non-invasive optoacoustic probing of the density and stiffness of single biological cells. J Appl Phys. https://doi.org/10.1063/1.4769294

26. Perrin B, Rossignol C, Bonello B, Jeannet JC (1999) Interferometric detection in picosecond ultrasonics. Phys B 263:571–573. https://doi.org/10.1016/S0921-4526(98)01479-3

27. Chigarev N, Rossignol C, Audoin B (2006) Surface displacement measured by beam distortion detection technique: application to picosecond ultrasonics. Rev Sci Instrum 77(11):114901. https://doi.org/10.1063/1.2372739

28. Liu P, Yi K, Sohn H (2021) Estimation of silicon wafer coating thickness using ultrasound generated by femtosecond laser. J Nondestruct Eval Diagn Progn Eng Syst 4(1):011005. https://doi.org/10.1115/1.4047673

29. Yi K, Liu P, Park SH, Sohn H (2022) Femtosecond laser ultrasonic inspection of a moving object and its application to estimation of silicon wafer coating thickness. Opt Lasers Eng 148:106778. https://doi.org/10.1016/j.optlaseng.2021.106778

30. Yu K, Devkota T, Beane G, Wang GP, Hartland GV (2017) Brillouin oscillations from single Au nanoplate opto-acoustic transducers. ACS Nano 11(8):8064–8071. https://doi.org/10.1021/acsnano.7b02703

31. Devos A, Le Louarn A (2003) Strong effect of interband transitions in the picosecond ultrasonics response of metallic thin films. Phys Rev B 68(4):045405. https://doi.org/10.1103/PhysRevB.68.045405

32. Dehoux T, Perton M, Chigarev N, Rossignol C, Rampnoux JM, Audoin B (2006) Effect of laser pulse duration in picosecond ultrasonics. J Appl Phys. https://doi.org/10.1063/1.2353751

33. Bartels A, Hudert F, Janke C, Dekorsy T, Köhler K (2006) Femtosecond time-resolved optical pump-probe spectroscopy at kilohertz-scan-rates over nanosecond-time-delays without mechanical delay line. Appl Phys Lett. https://doi.org/10.1063/1.2167812

34. Elzinga PA, Kneisler RJ, Lytle FE, Jiang Y, King GB, Laurendeau NM (1987) Pump/probe method for fast analysis of visible spectral signatures utilizing asynchronous optical sampling. Appl Opt 26(19):4303–4309. https://doi.org/10.1364/AO.26.004303

35. Abbas A, Guillet Y, Rampnoux JM, Rigail P, Mottay E, Audoin B, Dilhaire S (2014) Picosecond time resolved opto-acoustic imaging with 48 MHz frequency resolution. Opt Express 22(7):7831–7843. https://doi.org/10.1364/OE.22.007831

36. Pupeikis J, Willenberg B, Bruno F et al (2021) Picosecond ultrasonics with a free-running dual-comb laser. Opt Express 29(22):35735–35754. https://doi.org/10.1364/OE.440856

37. Vollmann J, Profunser DM, Dual J (2002) Sensitivity improvement of a pump–probe set-up for thin film and microstructure metrology. Ultrasonics 40(1–8):757–763. https://doi.org/10.1016/S0041-624X(02)00207-X

38. Liu P, Yi K, Park Y, Sohn H (2022) Ultrafast nonlinear ultrasonic measurement using femtosecond laser and modified lock-in detection. Opt Lasers Eng 150:106844. https://doi.org/10.1016/j.optlaseng.2021.106844

Jiaqi Dong received his Bachelor's degree from Tianjin University, Tianjin, China, in 2021. He is currently pursuing a Master's degree in optical engineering from Tianjin University. His research interests include femtosecond laser and precision measurements.

Chengyuan Yao received his Bachelor's degree from Shandong University, Shandong, China, in 2018. He is currently pursuing a PhD degree in instrument science and technology from Tianjin University. His research interests include precision spectroscopy techniques for micro-nano measurement.

Yuanhao Zhu received his Bachelor's degree in 2022. He is currently pursuing a Master's degree in the School of Precision Instruments and Optoelectronic Engineering, Tianjin University. His research interests are femtosecond laser and the application of femtosecond lasers in ranging.

Shaojie Li received his Bachelor's degree from Tianjin University, Tianjin, China, in 2021. He is currently pursuing a Master's degree in optoelectronic information engineering from Tianjin University. His research interests in femtosecond optical parametric oscillator.

Bowen Liu Associate Professor at Tianjin University. He received a B.S. degree and Ph.D. degree in optical engineering from Tianjin University in 2000 and 2009, respectively. He has worked on the femtosecond fiber laser system, coherent combination, and nonlinear fiber optics for many years, developed methods to accelerate the self-similar evolution in fiber amplifiers. His current research interests of femtosecond laser include coherent beam combination, pulse shaping, high-power fiber femtosecond laser system.

JinTao Fan received the B.S. degree in electronic science and technology and the Ph.D. degree in optical engineering from Tianjin University, Tianjin, China, in 2013 and 2019, respectively. After a postdoc at Leibniz University Hannover, he is currently an associate professor at School of Precision Instrument and Opto-electronics Engineering of Tianjin University, Tianjin, China. His research interests include optical parametric processes and structured beam generation.

Chunguang Hu Professor of School of Precision Instruments and Opto-Electronics Engineering, Tianjin University, China. He received the BS degree, the MS degree, and the PhD degree in Precision Instruments from Tianjin University in 2002, 2004, and 2007, respectively. From 2007 to 2010, He earned postdoctoral position at Johannes Kepler University Linz, Austria. His research interests include optical measurement for nano/micro-structures, optical tweezers based micromanipulation and force measurement.

Youjian Song received the BS degree in Electronic Science and Technology, in 2004, the PhD degree in Optical Engineering, in 2009, from Tianjin University, Tianjin, China. From 2009 to 2011, he was a postdoctoral fellow in KAIST, South Korea. He joined Tianjin University as an Associate Professor in 2011. Currently, he is a full professor in Tianjin University. He is a senior member of OPTICA and IEEE. His current research interests include optical frequency combs and precision measurements.

Minglie Hu received the BS degree in optoelectronics and the Ph.D. degree in optical engineering from Tianjin University, Tianjin, China, in 2000 and 2005, respectively. He is now a Full Professor at School of Precision Instrument and Opto-electronics Engineering, Tianjin University. He is the author of more than 200 peer-reviewed articles. His current research interests include mode-locking laser oscillators and amplifiers, fiber lasers, linear and nonlinear propagation in photonic crystal fibers, and microstructure optical devices.